Nanoscale Advances

ROYAL SOCIETY OF CHEMISTRY

PAPER

Published on 14 July 2026




Cite this: DOI: 10.1039/d6na00234j

# Film treatment–driven evolution of caesium lead bromide nanocrystals into layered 3D/2D $CsPbBr_3/CsPb_2Br_5$ heterostructures

Alice Fappani, [a] Francesca Pallini, [a] Valentina Bellotti,[a] Jayanta Dana,[b] Dhanushi Srinivasan,[b] Tero-Petri Ruoko, [b] Feng Wang, [c] Feng Gao [c] and Luca Beverina *[a]

Colloidal caesium lead bromide ($CsPbBr_3$) nanocrystals (NCs) are attractive building blocks for optoelectronic devices due to their high optical quality, compositional tunability, and processing versatility. However, post-deposition treatments required to improve film connectivity and charge transport can induce phase instability, most notably the transformation of $CsPbBr_3$ into the layered $CsPb_2Br_5$ phase. Here, we present a systematic investigation of how conventional thermal annealing, solvent washing, and ligand-exchange protocols applied to spin-coated $CsPbBr_3$ nanocrystal films drive the formation of mixed-dimensional $CsPbBr_3/CsPb_2Br_5$ heterostructures under ambient processing conditions. Using structural, morphological, and spectroscopic analyses, we show that solvent exposure—particularly when combined with mild thermal annealing—promotes the emergence of nanoscale $CsPb_2Br_5$ domains with treatment-dependent orientation and distribution. High-resolution electron microscopy confirms the intimate coexistence of the 3D and 2D phases within dense polycrystalline films. Steady-state and time-resolved optical spectroscopy, supported by femtosecond transient absorption measurements, reveal that controlled $CsPb_2Br_5$ formation can substantially enhance photoluminescence quantum yield and exciton lifetime by suppressing trap-assisted recombination, consistent with the formation of a type-I 3D/2D heterojunction. In contrast, treatments involving bifunctional additives may introduce additional trapping pathways, partially offsetting passivation benefits. Overall, this work clarifies the dual role of post-deposition processing in simultaneously enabling ligand removal and inducing phase transformation, demonstrating that $CsPb_2Br_5$ formation can be harnessed as a deliberate strategy to engineer interfacial passivation and improved carrier dynamics in $CsPbBr_3$ nanocrystal thin films.

Received 25th March 2026
Accepted 3rd July 2026

DOI: 10.1039/d6na00234j

rsc.li/nanoscale-advances

## Introduction

Perovskite materials have emerged as leading candidates in optoelectronics due to their excellent optical and transport properties, driving rapid growth in related research.[1,2] In particular, caesium lead bromide nanocrystals (NCs) stand out for their superior structural stability, enabling straightforward synthesis of a low-defective material with tailored properties.[3]

Three-dimensional $CsPbBr_3$ has been mainly employed in light-emitting and photodetection devices due to its easily achievable colour purity and strong luminescence.[4–6]

However, for energy-harvesting applications such as photovoltaics, lead halide perovskite (LHP) NCs remain less mature than microcrystalline films due to integration challenges. The ligand shell, while providing colloidal stability, hinders interfacial interactions and charge transport, and high grain-boundary densities introduce trap states.[7,8] Addressing these issues requires multiple depositions and post-processing steps to achieve adequate thickness, sintering, and ligand removal,[9–11] while using saturating additives to limit morphological damage and defects.[12–14]

Despite these limitations, NCs offer relevant advantages over *in situ*–grown microcrystalline layers, most notably: (1) independent optimization of synthesis and deposition conditions, (2) availability of up-scaled production methods of LHP NCs with consistent quality, paving the way to large-area deposition techniques,[15–17] (3) enhanced stability of corresponding devices,[18] and (4) higher sustainability, since environmentally concerning solvents such as DMF and DMSO can be avoided in both synthesis and processing.[19] As an additional benefit, we

[a]*Department of Materials Science, University of Milano-Bicocca, Milan I-20126, Italy. E-mail: luca.beverina@unimib.it*

[b]*Faculty of Engineering and Natural Sciences, Tampere University, Tampere, 33720, Finland*

[c]*Department of Physics, Chemistry, and Biology (IFM), Linköping University, Linköping 583 30, Sweden*

demonstrated that wastes coming from large-scale synthesis (up to 3.6 L of reaction volume) can be quantitatively recycled, thus avoiding unnecessary release of lead and volatile organic solvents.[20]

However, synthesis and post-deposition treatment of NCs still require investigation. Aside from challenges in the fabrication of devices, $CsPbBr_3$ nanocrystals can interconvert into different crystalline phases as a consequence of both thermal and chemical stimuli. The formation of the tetragonal $CsPb_2Br_5$ (a layered compound composed of isolated $[Pb_2Br_5]^{2-}$ units separated by $Cs^+$ ions) frequently competes with the synthesis and processing of the 3D $CsPbBr_3$.[21,22]

The effect on optical and transport properties—and thus on overall device performance—of the contamination of $CsPbBr_3$ NCs with $CsPb_2Br_5$ domains is a topic actively debated in the literature. Preliminary studies hinted at a positive effect of $CsPb_2Br_5$ impurities in $CsPbBr_3$ NCs leading to higher emission efficiencies with respect to pure $CsPbBr_3$.[23] However, Jiang *et al.*[24] demonstrated through computational analysis that $CsPb_2Br_5$ is an indirect-bandgap, photoluminescence (PL)-inactive material. Further experimental investigations confirmed its large bandgap of approximately 3.13 eV and a band-edge emission in the ultraviolet range, excluding the green emission observed for $CsPbBr_3$.[11,25] However, the apparent PL enhancement and increased carrier lifetime observed by others can be attributed to the coexistence of both $CsPbBr_3$ and $CsPb_2Br_5$ phases in composite or heterostructure systems. In such mixed systems, $CsPb_2Br_5$ can play a beneficial role by passivating surface defects, enhancing photostability, and modulating charge dynamics. Sun *et al.*[26] reported that $CsPb_2Br_5$ nanoparticles improve ionic conductivity, reduce exciton diffusion length, and lower trap density. Similarly, Zhang *et al.*[27] synthesized $CsPbBr_3/CsPb_2Br_5$ heterojunctions *via* post-synthesis solution treatment of $CsPbBr_3$ NCs, achieving enhanced optical properties and improved carrier kinetics owing to beneficial band alignment and interfacial coupling between the two phases. Such results highlight the critical role of controlling the nature of the heterojunction between the two phases in enhancing over worsening of the overall emissive efficiency of the material.

The evolution from $CsPbBr_3$ to $CsPb_2Br_5$ can occur through different synthetic pathways, including in-solution phase transformation during crystal growth,[23,26,28] post-synthesis solution treatment,[2,3,27,29–32] or solid-state conversion at elevated temperatures.[32] To sum up, $CsPbBr_3/CsPb_2Br_5$ nanocomposites, because of known applicative benefits, have been deliberately prepared either by direct synthesis or post-synthetic treatment of colloidal $CsPbBr_3$. Despite these advances, no systematic studies have been reported on the partial conversion of $CsPbBr_3$ thin films into $CsPb_2Br_5$ under standard device fabrication procedures. In such cases, the positive role of $CsPb_2Br_5$ should not be taken for granted, because structural, morphological and electronic specific interactions with the active $CsPbBr_3$ are intimately dependent on the post-deposition protocols. Understanding this phase transformation and its impact on the resulting optoelectronic properties is essential for optimizing material performance and stability in perovskite-based optoelectronic devices.

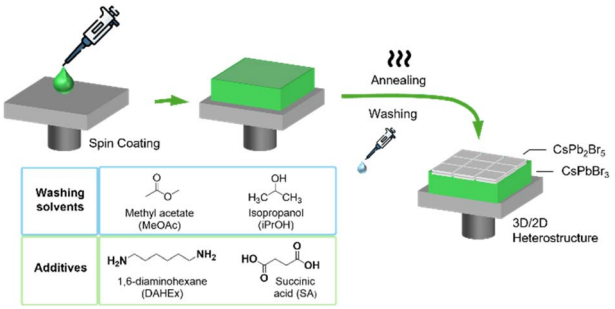


Scheme 1 Film treatments leading to surface modification of $CsPbBr_3$ to $CsPb_2Br_5$ and chemical structures of washing solvents and difunctional small molecules for the cross-linking of the NCs film.

We therefore carried out a systematic study of the effect of thermal annealing and/or exposure to chemical agents on spin-coated films of colloidal $CsPbBr_3$ NCs. We selected methyl acetate (MeOAc), commonly used in the literature,[33,34] and isopropanol (iPrOH), the antisolvent employed in our ligand-assisted reprecipitation (LARP) synthesis, to promote sintering and removal of excess oleylamine (OAm) ligands. In addition, we explored a post-deposition ligand exchange procedure aimed at replacing the native OAm/propionic acid (PA) assembly with small difunctional ligands: 1,6-diaminohexane (DAHex) and succinic acid (SA). To build a protocol of better compatibility with a potential industrial application, we processed $CsPbBr_3$ NCs in a laboratory atmosphere. Through this approach, we clarify how conventional post-deposition treatments for device fabrication can partially convert $CsPbBr_3$ into $CsPb_2Br_5$, yielding dual-phase $CsPbBr_3/CsPb_2Br_5$ films (Scheme 1). Aiming at a fundamental understanding of the phase interconversion process, we selected time-resolved photoluminescence and transient absorption spectroscopies to study the impact on overall exciton dynamics and its relation to structural changes. By understanding and tuning the treatment-dependent partial formation of a layered perovskite-related phase, this work provides preliminary guidelines on the processing of $CsPbBr_3$ NC-based films. In this paper, we show that while pre-annealing is beneficial for the film morphology, the choice of the washing protocol is fundamental to establishing an efficient surface passivation through the 2D layer. In this sense, a preference for less coordinating iPrOH over MeOAc and the avoidance of additives were found to induce a 3D/2D interface that favors the emissive efficiency of the film.

## Results and discussion

### Film formation and morphology

The deposition of $CsPbBr_3$ NC films was optimized by systematically adjusting spin-coating parameters and the number of deposited layers, aiming at dense and thick films, with minimal surface etching due to washing protocols. This essentially led to (i) privileging the good surface morphology and sufficient optical density yielded by a low spinning speed of 3 NCs layers;

(ii) acknowledging a stronger evolution of pristine nanoplateletss to thicker nanobricks in the film, similarly to what was already observed in aged inks,[20] as reflected by the modification in the absorption profile, induced by a longer exposition (static washing mode) to a polar solvent (Fig. S1–S3, SI). The optimized procedure yielded ten representative samples, selected for the analysis. These include pristine nanocrystal films (without any post-treatment), thermally annealed films (90 °C for 2 min), and films subjected to different post-deposition washing protocols. The washing treatments include exposure to isopropanol (iPrOH) or methyl acetate (MeOAc), both with and without bifunctional additives (1,6-diaminohexane (DAHex) and succinic acid (SA)), as well as washing preceded by a preliminary annealing step, again at 90 °C for 2 min. The complete list of samples and corresponding post-treatments is summarized in Table 1. The rationale behind this post-treatment design was to investigate the combined effects of annealing, solvent washing, and use of additives on nanocrystals sintering, surface etching, and ligand removal, while minimizing morphological degradation by tuning the additive concentration (Fig. S8). Conventional additives such as $Pb(OAc)_2$, FABr, and $Pb(SCN)_2$ (ref. 35–38) were initially tested but did not significantly improve film quality compared to simple solvent washing, although the FTIR spectra clearly hint that, whenever FABr is involved, $FA^+$ interacts with the NCs, as the C–N stretching of $FA^+$ arises at 1716 $cm^{-1}$ (Fig. S4). We thus turned to bifunctional additives, DAHex and SA, aiming at reducing the thickness of the insulating layer surrounding the NCs, while at the same time improving stability *via* crosslinking. The capability of acting as crosslinkers of difunctional ligands should not be given for granted. We tested several diamines (Scheme S1) in the starting ink, observing in all cases aggregation and flocculation that strongly hint at crosslinking (see dynamic light scattering analysis, Fig. S5). DAHex was selected because of the good quality of correlograms, with no sedimentation effects observed, and because of the equilibration of the dispersity to lower values, hinting at an homogeneous and stable ink with superior features compared to the dispersion treated with other diamines. Further evidence to DAHex effective interactions with NCs is provided by thermal gravimetric analysis (TGA), were the differentiation of the degradation profile reveals more efficacy in modifying the ligand shell (Fig. S6). While some control on overall aggregation could be traced to the chemical structure of the specific amines, even in the case of DAHex the effect was too strong to allow for the fabrication of films of good quality from a concentrated, pre-treated ink with the selected additive; in such a case, absorption profiles are unvaried and are only sensitive to slight changes in the film thickness depending on when the film is cast after the amine injection. Morphology is also affected, as time-dependent aggregates are visualized both micro- and macroscopically (Fig. S7). We thus introduced DAHex in a post-deposition step. For consistency, we introduced SA during post-treatment as well.

The different treatments led to distinct surface morphologies. Thermal annealing produced denser, more homogeneous films, whereas solvent washing induced varying degrees of damage. MeOAc washing generated elongated micrometre-scale cracks, while iPrOH treatment produced submicrometre-sized pinholes (Fig. 1a–d). Introducing a preliminary annealing step proved crucial for preserving film integrity during washing: both cracks and pinholes were significantly reduced or outright eliminated (Fig. 1e and f). Washing with solvents containing diluted DAHex or SA followed similar trends as the neat solvents, but the bifunctional ligands partially mitigated surface damage. Specifically, DAHex in MeOAc reduced the size and density of cracks, likely due to partial substitution of the bulky OAm with DAHex, compensating for the film shrinkage induced by the original ligand depletion. SA in iPrOH decreased the number of pinholes, reflecting a mild protective effect exerted by the bifunctional carboxylic ligand, again mitigating an abrupt stripping of the native capping (Fig. S9). Once again, preliminary annealing effectively prevented the surface etching, otherwise caused by solvents and additive solutions. The

Table 1 Post-treatments applied to air-processed OAm-capped $CsPbBr_3$ films

| Sample designation | Treatment 1 | Treatment 2 |
|---|---|---|
| Pristine | — | — |
| TA | Thermal annealing[a] | — |
| MW | MeOAc washing[b] | — |
| TA/MW | Thermal annealing | MeOAc washing |
| IW | iPrOH washing | — |
| TA/IW | Thermal annealing | iPrOH washing |
| DAHex | DAHex in MeOAc washing | — |
| TA/DAHex | Thermal annealing | DAHex in MeOAc washing |
| SA | SA in iPrOH washing | — |
| TA/SA | Thermal annealing | SA in iPrOH washing |

[a] Thermal annealing was run at 90 °C. [b] Washing was performed in the static mode.

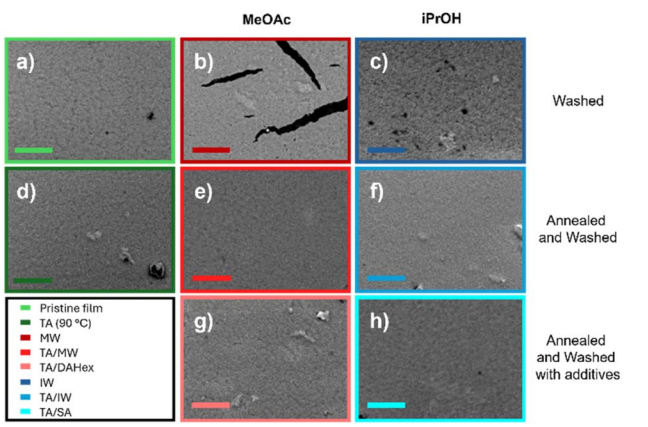


Fig. 1 SEM images of (a) pristine $CsPbBr_3$ NCs film and after washing with (b) MeOAc and (c) iPrOH; (d) $CsPbBr_3$ annealed at 90 °C for 2 min; pre-annealed films washed with (e) MeOAc and (f) iPrOH. Panels (g and h) show films washed with DAHex in MeOAc and SA in iPrOH, respectively, following preliminary annealing. The scale bar is 5 μm.

sintering of NCs, and, consequently, their reduced exposed surface area, reasonably made the film less sensitive to solvent-induced dissolution after the pre-annealing (Fig. 1g and h).

### Structural characterization

FT-IR spectroscopy confirmed the ligand removal upon washing for both unannealed and annealed films (Fig. 2b). The decrease of the intensity of the characteristic C–H stretching bands (2800–3000 $cm^{-1}$) associated with the long alkyl chains of OAm indicates the partial removal of surface ligands after treatment. However, quantification of ligand exchange with bifunctional additives was hindered by the spectral overlap of their vibrational fingerprints with the substrate.

X-ray diffraction (XRD) analysis (Fig. 2c and d) revealed that each processing route led to distinct outcomes in terms of crystalline phase composition—furtherly supported by evidences gathered with transmission electron microscopy techniques later in this work—and orientation, with $CsPbBr_3$ being either cubic or orthorhombic, along with signals arising from tetragonal $CsPb_2Br_5$ (Fig. S20); these aspects influenced the optical response and carrier dynamics of the films. Thermal annealing alone slightly improved crystallinity, as evidenced by the improvement in the signal-to-noise ratio in the corresponding diffractograms. In contrast, exposure to solvents consistently induced the formation of a secondary tetragonal $CsPb_2Br_5$ phase (peaks marked with stars in Fig. 2c and d), with peak intensity—taken as a qualitative indication of the relative amount of a specific phase—and orientation dependent on treatment. MeOAc washing promoted the appearance of $CsPb_2Br_5$ peaks; when preceded by annealing, the sample shows the presence of the tetragonal phase with comparable intensity, but a randomized orientation (arising of a fourth reflection at 47.88°). In contrast, iPrOH washing led to more $CsPb_2Br_5$ formation when annealing was applied beforehand. The absence of the fourth $CsPb_2Br_5$ peak at 47.88° in MW samples suggests that MeOAc promotes preferential orientation, likely due to surface interactions that generate lead-coordinating carboxylates,[39] possibly enhanced by MeOAc partial hydrolysis during in-air processing. Such specific interactions are likely to act differently with the morphological modification induced by the preliminary thermal annealing. We speculated that the interaction of DAHex with lead further enhanced orientation, showing only the 11.67° and 23.44° reflections. Preliminary annealing reduced $CsPb_2Br_5$ phase formation, consistently, again, with the reduced exposure of the nanocrystal surface.

The orientation effect, still present in the TA/DAHex film, confirmed the key role of the diamine in directing the phase formation. Conversely, SA in iPrOH slightly inhibited tetragonal phase formation, possibly due to limited perturbation of the ligand shell. SA is more similar to native PA in terms of molecular weight, and its interaction with the surface of NCs may be hindered by the shielding of the native bulky OAm, reducing the structural reorganization toward $CsPb_2Br_5$ (Fig. 2d). The appearance of the $CsPb_2Br_5$ tetragonal phase is plausibly ascribed to surficial CsBr depletion (Fig. 2a) induced

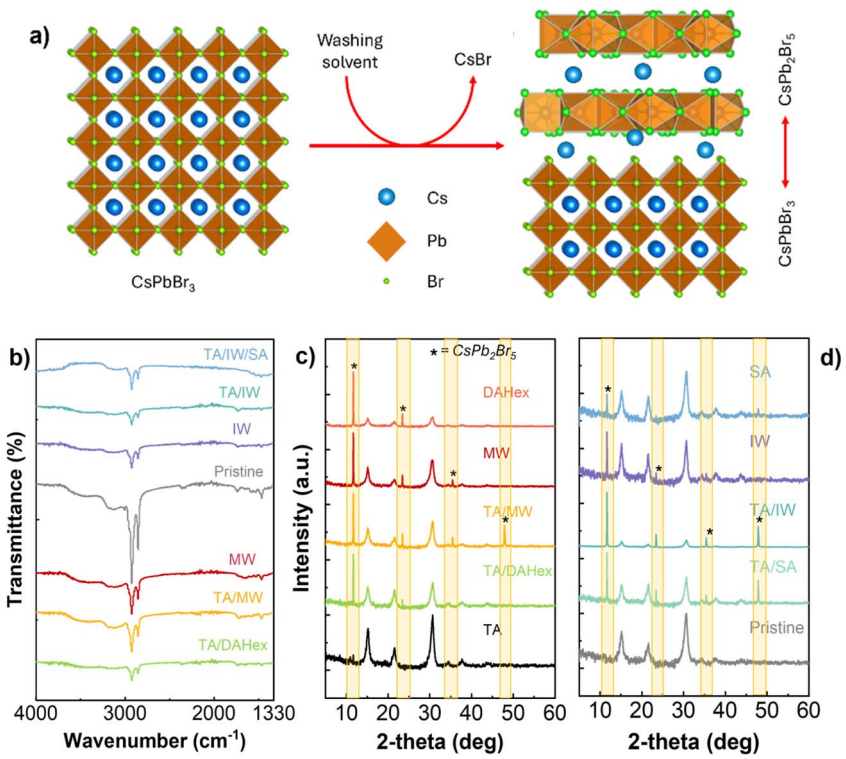


Fig. 2 (a) Depiction of hypothesized structural surface modification of perovskite nanomaterial. (b) FT-IR of pristine and treated $CsPbBr_3$ NCs films. XRD patterns of $CsPbBr_3$ NCs films after washing, pre-annealing, and washing with and without additives in (c) MeOAc and (d) iPrOH. The highlighted peaks, marked with (*), refer to the $CsPb_2Br_5$ phase.

by removal of ligands coordinated to surface-terminating $Cs^+$ and $Br^-$ after solvent exposure, an effect already observed on $CsPbBr_3$-related phases[35,36] ($2CsPbBr_3 \rightarrow CsPb_2Br_5 + CsBr$, with no microscopy and crystallographic evidence of the presence of CsBr in our films). Importantly, the secondary phase may act as a passivating barrier, protecting the 3D $CsPbBr_3$ from air and moisture. Furthermore, the formation of a $CsPbBr_3/CsPb_2Br_5$ heterojunction is known to enhance photoluminescence (PL) and exciton lifetime.[37] These findings provide a rational explanation for enhanced photophysical properties, often observed after post-deposition treatments aimed primarily at ligand removal and NC sintering.[38]

Since no distinct $CsPb_2Br_5$ crystallites were observed at the SEM resolution, nor did the TEM-EDS analysis detect compositional imbalances through the films (Fig. S11), the secondary phase is most likely present as nanoscale domains or thin layers coating the $CsPbBr_3$ nanocrystals.

To visualize the copresence of parent $CsPbBr_3$ and the secondary $CsPb_2Br_5$ phases and their distribution, we performed HR-TEM on a subset of samples, selecting washed films (with and without additives), always performing thermal annealing beforehand. The reason behind this choice is the superior morphology of this subset according to SEM characterization (Fig. 1).

In all four selected samples (Fig. 3a–d), high-resolution TEM imaging confirmed that both original $CsPbBr_3$ and $CsPb_2Br_5$ coexisted in thick and dense polycrystalline films, where individual nanoparticles were often too closely packed to be resolved (Fig. S16). The most populated *d*-spacings (5.8 Å and 2.7 Å) belonged to cubic and/or orthorhombic $CsPbBr_3$ (equivalent in terms of optical properties), followed by that of the tetragonal $CsPb_2Br_5$ (4.3 Å). Selected area electron diffraction (SAED) analysis highlighted the same main rings of polycrystalline films for each sample (Fig. S18 and 19), including diffraction rings consistent with the already mentioned interplanar distances (Fig. 3e). The derivation of *d*-spacings was repeated in different areas for statistics (Fig. S10, S12–15). The distribution of each crystalline domain appeared homogeneous in the short range in all cases, but with some morphological differences. With SA added to the washing iPrOH, or with MeOAc-based treatments, the shape of nanoparticles appeared to be slightly modified by a coating of $CsPb_2Br_5$ phase, while for the TA/IW sample, the composition is more uniform, with the two phases often superimposed and less distinguishable. Differences were also found in wide-field TEM images (Fig. S17). The iPrOH-treated samples (TA/IW and TA/SA, Fig. 3f–h) appeared comparatively of better quality than the ones exposed to MeOAc (TA/MW and TA/DAHex (Fig. 3g–i)). With additives in the washing solvent (Fig. 3h–i), dark inhomogeneities extending for hundreds of nanometres appeared, likely impacting carrier dynamics.

## Optical properties and charge carrier dynamics

To investigate the influence of different treatments on the photophysical properties of $CsPbBr_3$ films, detailed optical spectroscopic measurements were performed for all the film samples. Note that additives can influence the final properties of the films due to their efficiency in the native ligand exchange and the provided surficial passivation, based on the strength of their interactions with surficial LHP-NC atoms.[39,40] These effects are, however, difficult to disentangle from the ones produced by the structural rearrangement of the parent perovskite and were not investigated in our specific case. The removal of insulating ligands and the improved NCs packing contribute generally to a more favourable exciton dynamics together with the $CsPb_2Br_5$ passivating layer, but such effects act synergistically and reasonably coexist. Nonetheless, our simplified analysis

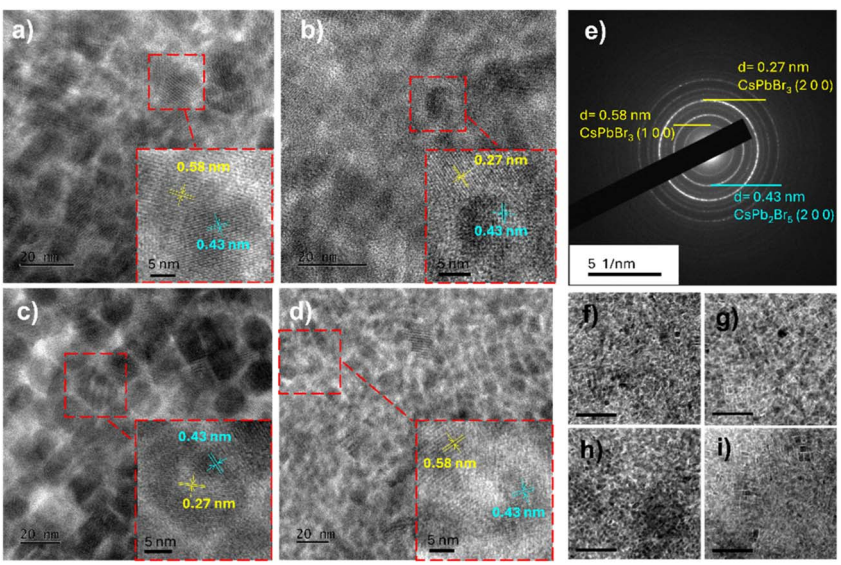


Fig. 3 HRTEM images with zoomed area and marked interplanar distances in the inserts of TA/IW (a), TA/MW (b), TA/SA (c), and TA/DAHex (d) samples; representative SAED pattern with diffraction rings corresponding to the most frequently found *d*-spacings (e). Wide-field TEM images of TA/IW (f), TA/MW (g), TA/SA (h), and TA/DAHex (i) samples (the scale bars are 100 nm).

focusing on the 2D phase formation yields consistent observations. Fig. 4a presents the steady-state absorption spectra of pristine and IW, SA, TA, TA/IW and TA/SA treated $CsPbBr_3$ films. The absorption spectra of films subjected to other treatments (MW, TA/MW, DAHex and TA/DAHex) are shown in Fig. S21. The pronounced band at ~510 nm corresponds to the first excitonic (band edge) transition that remains nearly identical after most treatments, indicating that the fundamental electronic structure is preserved. Notable exceptions are the TA/IW and TA/MW films, where the band edge exhibits a ~8 nm red shift relative to the pristine film. Although polar solvent washing- or thermal treatment-induced NCs sintering reasonably contributes to the red shift of the spectrum, these simple treatments alone do not produce a notable modification. Such a marked band edge shift is attributed to the formation of a 2D $CsPb_2Br_5$ layer on the $CsPbBr_3$ matrix. The resulting 3D/2D heterostructure possesses a type-I band alignment, leading to a partial delocalization of the electron wave function at the interface between $CsPb_2Br_5$ and $CsPbBr_3$.[27,41–43] In contrast, the formation of a heterostructure is less effective for the other treatments, resulting in a smaller change in the band structure. The normalized steady-state photoluminescence (PL) spectra of pristine $CsPbBr_3$ and films treated with IW, SA, TA, TA/IW and TA/SA following 400 nm excitation are presented in Fig. 4b.

In close analogy to the steady-state absorption results, the spectral shape and peak position are unchanged for most treatments, indicating preservation of the fundamental emissive state of $CsPbBr_3$. The normalized steady-state PL spectra subjected to other treatments (MW, TA/MW, DAHex and TA/DAHex) are shown in Fig. S21, with no distinct changes observed. The only exception is TA/IW, for which a few nm red-shift along with a slightly narrower emission band is displayed, indicating possible confinement of charge carriers due to the formation of the type-I heterostructure.[42,43]

To further elucidate the effect of post-treatment on the photophysical properties, time-resolved photoluminescence (TRPL) was measured with time-correlated single-photon counting to reveal the emission decay kinetics. All samples were excited at 405 nm and monitored at the maximum of the respective emission band. The PL decay traces of pristine and IW, SA, TA, TA/IW, and TA/SA films are shown in Fig. 4c. All decay traces were fitted using a three-exponential decay function, with the extracted intensity-weighted average TRPL lifetimes being 4.8, 18.2, 11.9, 13.0, 16.0, and 5.6 ns for pristine, IW, SA, TA, TA/IW, and TA/SA films, respectively (see Table S7 for all fitting results). For the pristine sample, the TRPL decay component lifetimes (relative amplitudes) were $t_1 = 0.75$ ns (62.5%), $t_2 = 3.49$ ns (33.1%), and $t_3 = 11.27$ ns (4.6%). In general, the dominant components, $t_1$ and $t_2$, are attributed to radiative electron–hole recombination from band-edge states,[44] while the minor long-lived component, $t_3$, is assigned to emissive recombination involving shallow trap states.[45] Upon treatment, substantial improvements are observed in the band-edge recombination lifetimes. For the IW-treated sample, $t_1$ and $t_2$

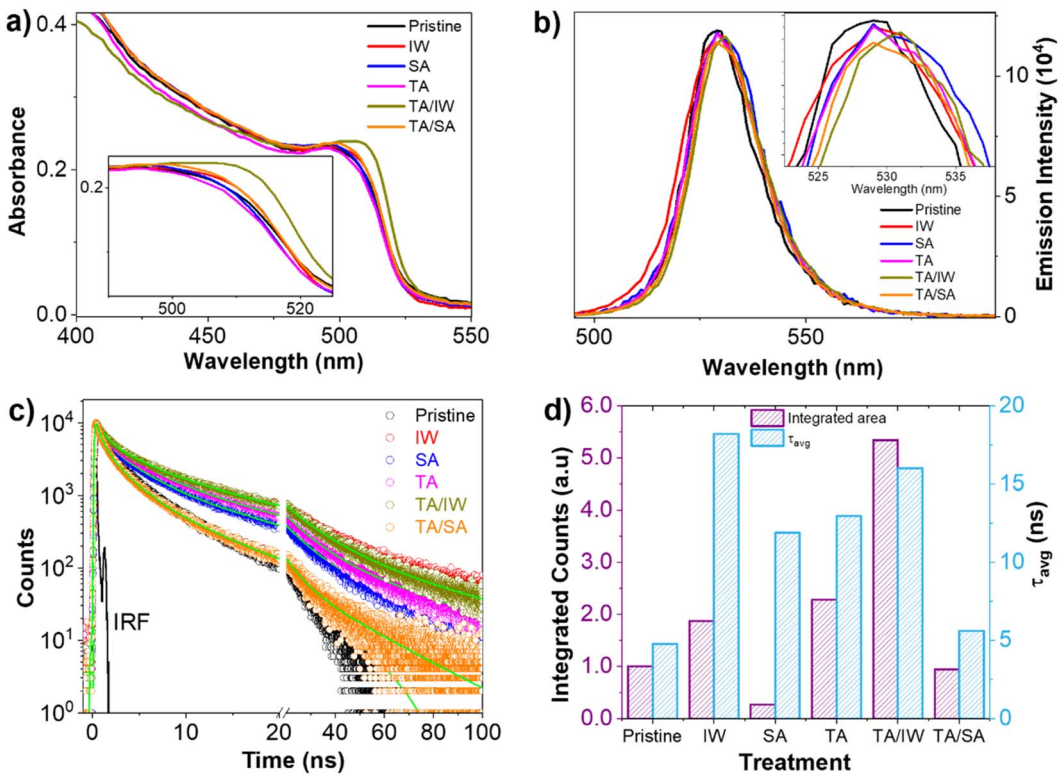


Fig. 4 (a) Steady-state absorption spectra, (b) steady-state emission spectra after 400 nm excitation, (c) TRPL decay kinetics after 405 nm excitation monitored at the emission band maximum (~530 nm), and (d) comparison of emission lifetime and integrated steady-state emission intensity of pristine, IW, SA, TA, TA/IW and TA/SA treated $CsPbBr_3$ films.

increase to 1.13 ns (62.1%) and 8.61 ns (32.2%), respectively, while for the TA-treated sample, they slightly change to 1.32 ns (62.3%) and 8.67 ns (33.9%). The combined TA/IW treated sample exhibits a further enhancement, with $t_1 = 1.78$ ns (72.7%) and $t_2 = 10.59$ ns (24.0%). These results indicate a significant suppression of non-radiative recombination pathways[46] and an enhancement of radiative band-edge recombination following TA treatment, with an even greater improvement observed for the combined TA/IW treatment.

Although the $t_3$ component also changes considerably compared with the pristine sample, its amplitude remains below 5% of the total decay. Therefore, its influence on the overall PLQY is expected to be relatively minor. Consequently, variations in the longest lifetime component do not necessarily translate into corresponding changes in PLQY, which is governed predominantly by the much larger contributions from the $t_1$ and $t_2$ components. The pronounced average lifetime enhancement observed upon post-treatment indicates a substantial suppression of nonradiative recombination pathways, consistent with improved surface morphology and interfacial passivation effects induced by the treatments.[42,43,47]

To correlate changes in relative emission quantum yield (QY) and TRPL lifetime to different treatments, we compiled both results to Fig. 4d. Since absolute quantum yield measurements are challenging for thin-film samples, relative emission QYs were determined by normalizing all emission intensities both with the absorbance at the excitation wavelength as well as to the integrated emission intensity of the pristine film that was taken as reference (set to unity). Despite the limitation of not having absolute data, we intended to compare samples prepared in the same conditions. We found the following order of relative emission QY: SA (0.26) < TA/SA (0.95) < pristine (1) < IW (1.9) < TA (2.3) < TA/IW (5.3), while the order of emission lifetime followed the trend pristine (4.8 ns) < TA/SA (5.6 ns) < SA (11.9 ns) < TA (13.0 ns) < TA/IW (16 ns) < IW (18.2 ns). This indicates that post-treatment significantly modifies the photophysical properties of the films by modifying the morphology and forming a passivating layer. The relative emission QY and lifetime of the thermally annealed film more than double relative to the pristine film, ascribed to improved crystallinity and reduced non-radiative recombination due to decreased trap concentration. On the other hand, the IW-treated film exhibits a nearly two-fold enhancement in relative emission QY and an approximately five-fold increase in PL lifetime compared to the pristine film. The effect is even more pronounced when IW is applied to a pre-annealed film (TA/IW), resulting in a ~5 times enhancement in relative emission QY and a ~4 times increase in PL lifetime relative to the pristine film and more than two-fold improvement in relative QY over the TA-treated film. SA-treatment decreases the relative QY from both pristine and annealed films, which is surprising since the SA-treatment is performed in iPrOH. Comparing SA and TA/SA films to the IW and TA/IW films shows that SA-treatment also decreases the lifetime compared to the nearest treatment. This indicates that SA treatment is harmful to the emission properties of the NC films.

The relative emission quantum yields and lifetimes for films subjected to other treatments (MW, TA/MW, DAHex and TA/DAHex) are presented in Fig. S23. Considering the pristine film as a reference, the order of emission QY follows TA/DAHex (0.35) < pristine (1) < TA/MW (1.2) < DAHex (1.6) < TA (2.3) < MW (2.4), while the corresponding TRPL lifetimes follow the order DAHex (2.5 ns) < TA/DAHex (4.1 ns) < pristine (4.7 ns) < MW (7.9 ns) < TA/MW (8.6 ns) < TA (13.0 ns). MW treatment promotes the formation of the 2D layer, resulting in QY increasing to 2.4 times that of the pristine film. However, the thermal annealing prior to MW treatment reduces this enhancement, indicating a less effective heterostructure formation. Unlike SA, DAHex improves the emission QY over the pristine sample, although the emission lifetime decreases. Nevertheless, DAHex-treated samples also have shorter emission lifetimes and lower emission QY than the respective pure solvent-treated samples (Fig. S21 and S22).

Overall, the trends in QY and TRPL lifetime are broadly consistent. The longest lifetime component ($\tau_3$) of Table S7, with minor contribution to the total decay amplitude, is attributed to recombination through reversible (shallow) trap states.[48,49] Different surface treatments modify the population of these shallow traps to varying degrees, leading to small changes in the $\tau_3$ contribution and the overall PL lifetime. Since $\tau_3$ represents only a minor fraction of the total emission and originates from trap-mediated recombination, its variation has a limited impact on PLQY. Consequently, the sample with the longest PL lifetime does not necessarily exhibit the highest PLQY, which is primarily governed by the dominant band-edge recombination processes. The 2D layer of $CsPb_2Br_5$ acts as an effective passivating layer for $CsPbBr_3$, resulting in suppressed nonradiative recombination and substantially enhanced photophysical properties.[47,50] The TA sample has high emission QY and lifetime due to the sintering improving the film crystallinity, whereas the highest QY and lifetime are observed for TA/IW treatment due to iPrOH washing removing unwanted ligands from the NC surface and inducing a pronounced $CsPb_2Br_5$ formation. This effect is not observed with the TA/MW sample, which has a lower QY and a faster lifetime due to the weaker heterostructure formation. Furthermore, additives like SA or DAHex introduce additional trapping channels, facilitating non-radiative recombination and decreasing the emissive properties of the NC films. Note that the chemical nature of additive-induced defects was not directly probed.

To explore the influence of different treatments on charge carrier dynamics, we performed femtosecond transient absorption (fs-TA) experiments following 400 nm excitation. The fs-TA spectra of the pristine $CsPbBr_3$ film at different delay times are presented in Fig. 5a and the 2D fs-TA spectra for all samples are presented in Fig. S23–S25. The spectral features for all samples resemble the pristine film, illustrating the unchanged nature of the bulk semiconducting material. For all materials, a photoinduced bleach (PB) centered at 515 nm is flanked by two photoinduced absorption bands PA1 and PA2. The PB originates from a decrease in the magnitude of the band-edge excitonic transition after exciton generation. The ultrafast PA1 transient absorption band is attributed to a bi-

 

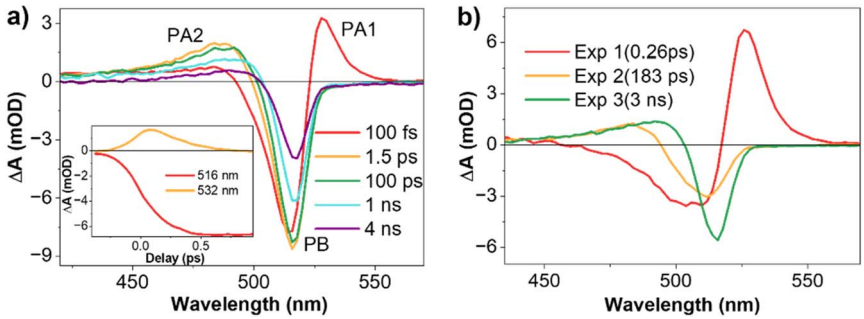


Fig. 5 (a) fs-TA spectra of pristine film at different time delays following 400 nm excitation with variation of the absorption at fixed wavelengths in the insert. (b) DAS of pristine film.

exciton shift arising from interactions between hot excitons generated by the pump and band-edge excitons generated by the probe beams. The fast decay of PA1 is accompanied by a concomitant growth of the PB signal, as shown in the inset of Fig. 5a, representing the carrier cooling process of the hot carriers generated by the 400 nm excitation.[51,52]

Photoexcited charge carriers can undergo multiple relaxation pathways with distinct lifetimes that must be resolved to explore the impacts of different treatments on the $CsPbBr_3$ charge-carrier dynamics. Therefore, we fitted the fs-TA spectra globally using tri-exponential fitting (details in SI) and present the decay-associated spectra (DAS) of pristine $CsPbBr_3$ in Fig. 5b. The ultrafast 260 fs lifetime component exhibits the decay of PA1 and growth of PB, attributed to carrier cooling. The intermediate 183 ps lifetime component is assigned to a carrier trapping process, while the long lifetime 3 ns component corresponds to band edge exciton recombination.[53] The fs-TA spectra of all treated samples were globally fitted using the same fitting method and the corresponding DAS of IW, SA, TA, TA/IW, and TA/SA treated $CsPbBr_3$ are presented in Fig. S26. The fast lifetime carrier cooling components are nearly identical, with lifetimes close to 300 fs. This component remains nearly unchanged across all samples, indicating that the initial relaxation of hot carriers is largely unaffected by the surface treatments. The intermediate lifetime carrier trapping components are close to 180 ps; however, the amplitudes vary due to the influence of surface treatments. The intermediate lifetime DAS normalized to the maximum signal of the bi-exciton shift (PA1), which is directly proportional to the average number of generated excitons, are shown in Fig. 6a. A decrease in the trapping-related component is observed in the order: pristine > TA > TA/SA > SA > IW > TA/IW. To quantify the decrease more clearly, we have integrated the DAS amplitude and show the integrated amplitudes in Fig. 6b. The total amplitude of the trapping component can be correlated with trap density and is consistent with our emission QY and lifetime measurements.

For the IW and TA treated samples, the amplitude contribution of the second component is significantly reduced compared to the pristine sample, indicating lower trapping probability and a suppression of non-radiative carrier losses. This behaviour is consistent with the TRPL results, where the dominant radiative lifetime components ($t_1$ and $t_2$) increase substantially after treatment. Furthermore, the trapping contribution decreases even more for the TA/IW-treated sample, which directly mirrors the additional enhancement observed in the PLQY.

A similar correlation is observed for the SA and TA/SA-treated samples. Relative to the pristine sample, the trapping-related contribution in the TA data is reduced, while the dominant radiative lifetime components in the TRPL measurements become longer. These observations collectively demonstrate a clear relationship between the TA and TRPL results: surface treatment suppresses carrier trapping and non-radiative recombination, thereby increasing the population of carriers

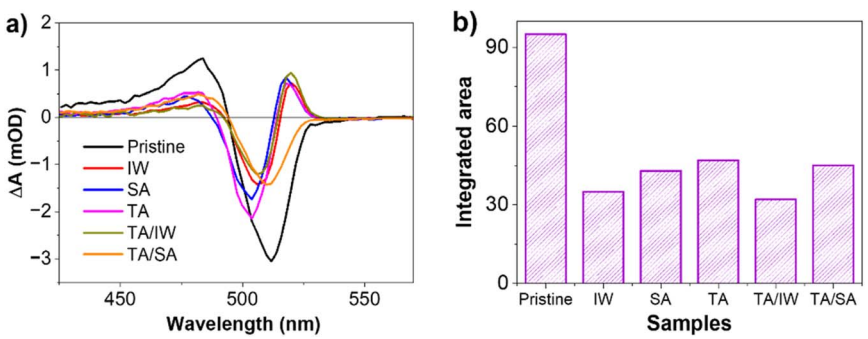


Fig. 6 Normalized DAS for intermediate lifetime carrier trapping of pristine, IW, SA, TA, TA/IW and TA/SA $CsPbBr_3$ samples; (b) comparison of integrated DAS amplitude of the intermediate lifetime carrier trapping.

Table 2 Changes in $CsPb_2Br_5$ formation, orientation, relative PLQY, TRPL, and TAS trap amplitude. The symbol (—) indicates unvaried properties compared to the reference. The free arrow indicates increasing or decreasing trend *vs.* the pristine sample, whereas the arrow in parentheses indicates a change from the most comparable treatment: IW for SA, MW for DAHex, TA for TA/IW & TA/MW, TA/IW for TA/SA, and TA/MW for TA/DAHex

| Sample | $CsPb_2Br_5$ formation, orientation | PLQY | TRPL | TAS trap amplitude |
|---|---|---|---|---|
| Pristine | — | — | — | — |
| IW | Slightly, oriented | ↑ | ↑ | ↓ |
| SA | Slightly, random orientation | ↓(↓) | ↑(↓) | ↓(↑) |
| MW | Present, oriented | ↑ | ↑ | ↓ |
| DAHex | Present, oriented | ↑(↓) | ↓(↓) | ↓(–) |
| TA | Not present | ↑ | ↑ | ↓ |
| TA/IW | Pronounced, random orientation | ↑(↑) | ↑(↑) | ↓(↓) |
| TA/SA | Present, random orientation | ↓(↓) | ↑(↓) | ↓(↑) |
| TA/MW | Present, random orientation | ↑(↓) | ↑(↓) | ↑(↓) |
| TA/DAHex | Present, oriented | ↓(↓) | ↓(↓) | ↓(↑) |

available for radiative band-edge recombination. Consequently, the reduced trapping observed in TAS is directly reflected in the longer radiative lifetimes and enhanced PLQY measured by TRPL and steady-state photoluminescence.[46,48,54]

The fs-TA data of MW, TA/MW, DAHex and TA/DAHex were also globally fitted using the same tri-exponential model, and the corresponding DAS are shown in Fig. S27. The fastest components associated with hot carrier cooling remain nearly constant at 300 fs. The intermediate DAS corresponding to carrier trapping exhibits lifetimes of 165 ps, 200 ps, 161 ps for MW, TA/MW, DAHex, respectively. These values are comparable to those of pristine $CsPbBr_3$, however, for TA/DAHex, the trapping component is significantly faster at 59 ps. This is also consistent with the TRPL results, where both DAHex-treated films have the fastest emission lifetimes. The amplitudes of the intermediate lifetime trapping components are lower than for the pristine sample, as shown in Fig. S28.[55–60]

The reduction in trapping contribution follows the trend observed in the emission QY measurements. This behaviour is consistent with the observed PL characteristics and further supports the correlation between reduced trap density and improved charge-carrier dynamics in treated $CsPbBr_3$ films.

These observations can be rationalized by considering the formation of the $CsPbBr_3/CsPb_2Br_5$ heterojunction. The 2D $CsPb_2Br_5$ phase, with its wider bandgap, can passivate the $CsPbBr_3$ phase, thereby enhancing PL intensity and extending the exciton lifetimes.

The overall effects of all treatments on the photophysical properties are summarized in Table 2. The thermal treatment (TA), washing (IW and MW), and their combination (TA/MW and TA/IW) significantly improved the relative PLQY and lifetime compared to the pristine film. This enhancement can be attributed to the formation of a passivating layer on the NC film surface, with TA/IW showing the largest improvement due to the pronounced heterojunction formation. However, in samples with difunctional additives (*e.g.* SA, DAHex, TA/DAHex, TA/SA), the additives appear to increase the amount of surface trapping pathways. We assume that in such cases increased defectivity induced by solvent treatments is not effectively compensated by oriented/inhomogeneous crystallization of $CsPb_2Br_5$, resulting in less favourable exciton dynamics. Overall, the combination of PL, TRPL, and fs-TA suggests that both surface passivation and proper heterojunction formation contribute to the optical performance, with the balance between these mechanisms being strongly dependent on solvent choice, additive type, and annealing history.

## Conclusions

In this work, we have systematically elucidated how standard post-deposition treatments commonly employed in the fabrication of $CsPbBr_3$ nanocrystal thin films can drive a partial and controllable phase transformation toward the layered $CsPb_2Br_5$ phase, ultimately yielding mixed-dimensional $CsPbBr_3/CsPb_2Br_5$ heterostructures. Potential benefits from a $CsPb_2Br_5$ coating are known, but its formation through post-deposition treatments is not usually the primary aim. We integrated information from XRD, HR-TEM, SEM, FTIR, PL, TRPL and femtosecond transient absorption measurements to establish a correlation between processing protocols, structural modifications and exciton dynamics.

By combining thermal annealing, solvent washing, and ligand-exchange strategies under ambient processing conditions, we demonstrate that even mild and widely used protocols profoundly affect film morphology, crystalline phase composition, and interfacial structure.

Structural analyses reveal that solvent exposure—particularly when coupled with annealing—promotes the formation of nanoscale $CsPb_2Br_5$ domains, often with preferential orientation depending on solvent chemistry and the presence of bifunctional additives. High-resolution electron microscopy confirms the intimate coexistence of the 3D and 2D phases within dense polycrystalline films, strongly suggesting the formation of heterojunctions rather than macroscopic phase segregation. Importantly, preliminary thermal annealing mitigates morphological degradation during washing, enabling the formation of compact films while modulating the extent (qualitatively evaluated basing on relative intensity of signals for $CsPbBr_3$ and the derived tetragonal phase without an absolute quantification) and orientation of $CsPb_2Br_5$ formation.

Optical spectroscopy and ultrafast spectroscopy collectively show that these structural modifications have a decisive impact on exciton dynamics. Treatments that favour the formation of a well-coupled 3D/2D $CsPbBr_3/CsPb_2Br_5$ interface—most notably the combination of annealing followed by iPrOH washing—lead to pronounced enhancements in photoluminescence quantum yield, extended emission lifetimes, and a substantial reduction of trap-assisted recombination, as directly evidenced by transient absorption measurements. In contrast, treatments that induce excessive orientation or introduce additional defect states *via* additives result in less effective passivation and diminished photophysical benefits.

Overall, our results demonstrate that the emergence of $CsPb_2Br_5$ during post-deposition processing should not be regarded merely as an undesirable side reaction, but rather as a tuneable outcome that can be exploited to engineer beneficial heterostructures at the nanoscale. This work provides a unifying framework linking processing conditions, phase evolution, and charge-carrier dynamics in $CsPbBr_3$ nanocrystal films, offering practical guidelines for optimizing their optoelectronic performance. These insights are expected to be broadly relevant for the rational design of nanocrystal-based perovskite devices, where controlled mixed-dimensional architectures can be leveraged to enhance efficiency, stability, and reproducibility.

## Author contributions

Conceptualization: A. F., L. B. investigation: A. F., F. P., V. B., J. D., D. S. data curation: A. F., J. D. supervision: L. B., T.-P. R., F. G. writing – original draft: A. F., V. B., F. P., J. D. writing – review and editing: T.-P. R., L. B., F. W. funding acquisition: L. B., F. G.

## Conflicts of interest

There are no conflicts to declare.

## Data availability

The data supporting this article have been included as part of the supplementary information (SI). Supplementary information is available. See DOI: https://doi.org/10.1039/d6na00234j.

## Acknowledgements

Funding from MUR (project InPOWER grant no P2022PXS5S) is gratefully acknowledged. L. B. acknowledges the MUSA – Multilayered Urban Sustainability Action – project, funded by the European Union – NextGenerationEU, under the National Recovery and Resilience Plan (NRRP) Mission 4 Component 2 Investment Line 1.5: Strengthening of research structures and creation of R&D "innovation ecosystems", set up of "territorial leaders in R&D". F. P. acknowledges project RePLACE (grant no 2022C4YNP8). T.-P. R. acknowledges support from the Research Council of Finland Academy Researcher Fellowship (Fluorocage, no. 363033), the Finnish Centre of Excellence program on Life Inspired Hybrid Materials Research (LIBER, no. 346107), and the Finnish Flagship program on Photonics Research and Innovation (PREIN, no. 320165).

## References

1 A. S. Shikoh and A. Polyakov, *Phys. Status Solidi A Appl. Mater. Sci.*, 2020, **217**, 2000441.
2 A. Fakharuddin, M. K. Gangishetty, M. Abdi-Jalebi, S. H. Chin, A. R. bin Mohd Yusoff, D. N. Congreve, *et al.*, *Nat. Electron.*, 2022, **5**, 203–216.
3 Y. Chen, X. Liu, T. Wang and Y. Zhao, *Acc. Chem. Res.*, 2021, **54**, 3452–3461.
4 C. Collantes, W. Teixeira, V. González Pedro, M. J. Bañuls and Á. Maquieira, *Appl. Mater. Today*, 2023, **31**, 101775.
5 P. Meredith and A. Armin, *Nature*, 2018, **562**, 197–198.
6 K. Sakhatskyi, A. Bhardwaj, G. J. Matt, S. Yakunin and M. V. Kovalenko, *Adv. Mater.*, 2025, **37**, 2418465.
7 M. F. Lichtenegger, J. Drewniok, A. Bornschlegl, C. Lampe, A. Singldinger, N. A. Henke, *et al.*, *ACS Nano*, 2022, **16**, 6317–6324.
8 G. W. P. Adhyaksa, S. Brittman, H. Āboliņš, A. Lof, X. Li, J. D. Keelor, *et al.*, *Adv. Mater.*, 2018, **30**, 1804792.
9 X. Zhang, H. Huang, C. Zhao, L. Jin, C. Lee, Y. Li, *et al.*, *Nat. Energy*, 2024, **9**, 1378–1387.
10 X. Zhang, H. Huang, X. Ling, J. Sun, X. Jiang, Y. Wang, *et al.*, *Adv. Mater.*, 2022, **34**, 2105977.
11 J. B. Hoffman, G. Zaiats, I. Wappes and P. V. Kamat, *Chem. Mater.*, 2017, **29**, 9767–9774.
12 J. Kim, B. Koo, W. H. Kim, J. Choi, C. Choi, S. J. Lim, *et al.*, *Nano Energy*, 2019, **66**, 104130.
13 C. Liu, Q. Zeng, Y. Zhao, Y. Yu, M. Yang, H. Gao, *et al.*, *Sol. RRL*, 2020, **4**, 2000102.
14 E. M. Sanehira, A. R. Marshall, J. A. Christians, S. P. Harvey, P. N. Ciesielski, L. M. Wheeler, *et al.*, *Sci. Adv.*, 2017, **3**, eaao4202.
15 D. Dou, H. Sun, C. Li, S. Gan and L. Li, *Adv. Funct. Mater.*, 2024, **34**, 2314398.
16 Y. Xiao, C. Zuo, J. X. Zhong, W. Q. Wu, L. Shen and L. Ding, *Adv. Energy Mater.*, 2021, **11**, 2100378.
17 K. Bruening, B. Dou, J. Simonaitis, Y. Y. Lin, M. F. A. M. van Hest and C. J. Tassone, *Joule*, 2018, **2**, 2464–2476.
18 A. Hazarika, Q. Zhao, E. Ashley Gaulding, J. A. Christians, B. Dou, A. R. Marshall, *et al.*, *ACS Nano*, 2018, **12**, 10327–10337.
19 Q. A. Akkerman, M. Gandini, F. Di Stasio, P. Rastogi, F. Palazon, G. Bertoni, *et al.*, *Nat. Energy*, 2017, **2**, 16194.
20 S. Mecca, F. Pallini, V. Pinchetti, A. Erroi, A. Fappani, F. Rossi, *et al.*, *ACS Appl. Nano Mater.*, 2023, **6**, 9436–9443.
21 A. Swarnkar, V. K. Ravi and A. Nag, *ACS Energy Lett.*, 2017, **2**, 1089–1098.
22 S. K. Balakrishnan and P. V. Kamat, *Chem. Mater.*, 2018, **30**, 74–78.
23 J. Li, H. Zhang, S. Wang, D. Long, M. Li, Y. Guo, *et al.*, *RSC Adv.*, 2017, **7**, 54002–54007.
24 G. Li, H. Wang, Z. Zhu, Y. Chang, T. Zhang, Z. Song, *et al.*, *Chem. Commun.*, 2016, **52**, 11296–11299.

 

25 V. Drushliak and M. Szafrański, *Inorg. Chem.*, 2022, **61**, 14389–14396.
26 X. Zhang, B. Xu, J. Zhang, Y. Gao, Y. Zheng, K. Wang, *et al.*, *Adv. Funct. Mater.*, 2016, **26**, 4595–4600.
27 Z. P. Huang, B. Ma, H. Wang, N. Li, R. T. Liu, Z. Q. Zhang, *et al.*, *J. Phys. Chem. Lett.*, 2020, **11**, 6007–6015.
28 P. Song, B. Qiao, D. Song, Z. Liang, D. Gao, J. Cao, *et al.*, *J. Alloys Compd.*, 2018, **767**, 98–105.
29 W. Shen, L. Ruan, Z. Shen and Z. Deng, *Chem. Commun.*, 2018, **54**, 2804–2807.
30 Y. Li, X. Yang and A. Xie, *J. Lumin.*, 2021, **236**, 118154.
31 S. Sahu, T. Debnath and K. Sahu, *J. Phys. Chem. Lett.*, 2024, **15**, 3677–3682.
32 F. Palazon, S. Dogan, S. Marras, F. Locardi, I. Nelli, P. Rastogi, *et al.*, *J. Phys. Chem. C*, 2017, **121**, 11956–11961.
33 A. Swarnkar, A. R. Marshall, E. M. Sanehira, B. D. Chernomordik, D. T. Moore, J. A. Christians, *et al.*, *Science*, 2016, **354**, 88–92.
34 H. S. Yang, D. Lee, E. H. Suh, S. H. Noh, K. H. Lee, J. G. Oh, *et al.*, *Chem. Eng. J.*, 2023, **457**, 141107.
35 H. S. Yang, E. H. Suh, S. H. Noh, J. Jung, J. G. Oh, K. H. Lee, *et al.*, *Chem. Eng. J.*, 2023, **454**, 140331.
36 M. A. Reus, A. Krifa, Q. A. Akkerman, A. Biewald, Z. Xu, D. P. Kosbahn, *et al.*, *Adv. Opt. Mater.*, 2024, **12**, 2301008.
37 X. Ling, J. Yuan, X. Zhang, Y. Qian, S. M. Zakeeruddin, B. W. Larson, *et al.*, *Adv. Mater.*, 2020, **32**, 2001906.
38 Y. Sun, J. Peng, Y. Chen, Y. Yao and Z. Liang, *Sci. Rep.*, 2017, **7**, 46193.
39 F. Palazon, C. Urso, L. De Trizio, Q. Akkerman, S. Marras, F. Locardi, *et al.*, *ACS Energy Lett.*, 2017, **2**, 2445–2448.
40 S. K. Balakrishnan and P. V. Kamat, *Chem. Mater.*, 2018, **30**, 74–78.
41 V. Naresh, S. Singh, H. Soh, J. Lee and N. Lee, *Mater. Today Nano*, 2023, **23**, 100364.
42 C. S. Jo, K. Noh, S. H. Noh, H. Yoo, Y. Kim, J. Jang, *et al.*, *ACS Appl. Nano Mater.*, 2020, **3**, 11801–11810.
43 S. Narra, P. S. Liao, S. S. Bhosale and E. W. G. Diau, *Nanomaterials*, 2023, **13**, 1718.
44 F. Zaccaria, B. Zhang, L. Goldoni, M. Imran, J. Zito, B. Van Beek, *et al.*, *ACS Nano*, 2022, **16**, 1444–1455.
45 R. T. Liu, X. P. Zhai, Z. Y. Zhu, B. Sun, D. W. Liu, B. Ma, *et al.*, *J. Phys. Chem. Lett.*, 2019, **10**, 6572–6577.
46 J. Cho, Y. K. Jung, J. K. Lee and H. S. Jung, *Langmuir*, 2017, **33**, 3711–3719.
47 J. Hao, H. Liu, J. Miao, R. Lu, Z. Zhou, B. Zhao, *et al.*, *Sci. Rep.*, 2019, **9**, 12048.
48 V. S. Chirvony and J. P. Martínez-Pastor, *J. Phys. Chem. Lett.*, 2018, **9**, 4955–4962.
49 M. Abdellah, K. J. Karki, N. Lenngren, K. Zheng, T. Pascher, A. Yartsev, *et al.*, *J. Phys. Chem. C*, 2014, **118**, 21682–21686.
50 W. Van Der Stam, G. Grimaldi, J. J. Geuchies, S. Gudjonsdottir, P. T. Van Uffelen, M. Van Overeem, *et al.*, *Chem. Mater.*, 2019, **31**, 8484–8493.
51 J. Zhang, C. Li, J. Li and X. Peng, *Chem. Mater.*, 2023, **35**, 7049–7059.
52 K. E. Knowles, E. A. McArthur and E. A. Weiss, *ACS Nano*, 2011, **5**, 2026–2035.
53 B. A. Koscher, J. K. Swabeck, N. D. Bronstein and A. P. Alivisatos, *J. Am. Chem. Soc.*, 2017, **139**, 6566–6569.
54 A. Pandey and P. Guyot-Sionnest, *Science*, 2008, **322**, 929–932.
55 J. Dana, T. Binyamin, L. Etgar and S. Ruhman, *ACS Nano*, 2021, **15**, 9039–9047.
56 T. Ghosh, S. Aharon, A. Shpatz, L. Etgar and S. Ruhman, *ACS Nano*, 2018, **12**, 5719–5725.
57 J. Dana, M. R. Ajayakumar, A. Efimov, T. Weckman, K. Honkala and N. V. Tkachenko, *Nanoscale*, 2024, **16**, 20725–20737.
58 C. T. Smith, M. A. Leontiadou, R. Page, P. O'Brien and D. J. Binks, *Adv. Sci.*, 2015, **2**, 1500088.
59 A. Stelmakh, M. Aebli, A. Baumketner and M. V. Kovalenko, *Chem. Mater.*, 2021, **33**, 5962–5973.
60 N. V. Tkachenko, *ChemPhotoChem*, 2018, **2**, 112–120.

 